Phase Transformation Behavior and Stability of $LiNiO_2$ Cathode Material for Li-Ion Batteries from In Situ Pressure and Gas Analysis and Operando X-Ray Diffraction

Dr. Lea de Biasi,[a], [b], * Alexander Schiele,[a] Dr. Maria Roca-Ayats,[a], [c] Dr. Grecia Garcia,[a] Dr. Torsten Brezesinski,[a], * Dr. Pascal Hartmann,[a], [d], * and Prof. Jürgen Janek[a], [e]

[a] Battery and Electrochemistry Laboratory, Institute of Nanotechnology, Karlsruhe Institute of Technology (KIT), Hermann-von-Helmholtz-Platz 1, 76344 Eggenstein-Leopoldshafen, Germany

E-mail: lea.biasi@kit.edu, torsten.brezesinski@kit

[b] Institute for Applied Materials, Karlsruhe Institute of Technology (KIT), Hermann-von-Helmholtz-Platz 1, 76344 Eggenstein-Leopoldshafen, Germany

[c] Physical Chemistry Department, Faculty of Chemistry, University of Santiago de Compostela, Rúa de José María Suárez Núñez 3, 15782 Santiago de Compostela, Spain

[d] BASF SE, Carl-Bosch-Straße 38, 67056 Ludwigshafen, Germany.

E-mail: pascal.hartmann@basf.com

[e] Institute of Physical Chemistry & Center for Materials Research, Justus-Liebig-University Giessen, Heinrich-Buff-Ring 17, 35392 Giessen, Germany

Table of Contents

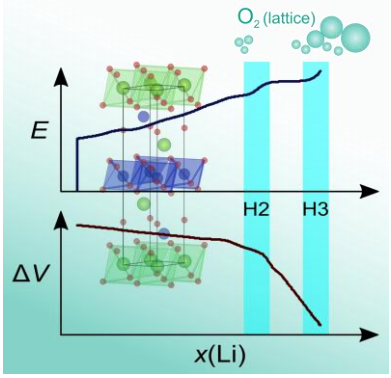

New insights into the structural evolution, the gassing behavior, and the cycling stability of $LiNiO_2$, a promising next-generation cathode active material for use in Li-ion batteries, are gained from the combination of electrochemical charge/discharge experiments with different in situ analytical tools, such as X-ray diffraction and differential electrochemical mass spectrometry.

Abstract

Ni-rich layered oxide cathode materials, in particular the end member $LiNiO_2$, suffer from drawbacks of high surface reactivity and severe structural changes with de-/lithiation, leading to accelerated degradation and limiting practical implementation of these otherwise highly promising electrode materials in Li-ion batteries. Among all known phase transformations occurring in $LiNiO_2$, that from the H2 to H3 phase at high state of charge is believed to have the most detrimental impact on the material's stability. In this work, the multistep phase transformation process and associated effects are analyzed by galvanostatic cycling, operando X-ray diffraction, and in situ pressure and gas analysis. The combined results provide thorough insights into the structural changes and how they affect the stability of $LiNiO_2$. During the H2-H3 transformation, $LiNiO_2$ experiences the most significant changes in *c*-lattice parameter, and therefore, large mechanical stress. As for electrochemical stability, $LiNiO_2$ suffers strongly in the H3 region. Oxygen evolution is observed not only during charge, but also during discharge and found to be correlated with the presence of the H2 and H3 phases. Taken together, our experimental data help better understand the degradation processes and inherent instability of $LiNiO_2$ in Li-ion cells when operated above around 75% state of charge.

Keywords

Electrochemistry, lithium-ion battery, lithium nickel oxide, oxygen release, structure elucidation

Introduction

During the 1990s, $LiNiO_2$ (LNO) was considered the most promising cathode active material (CAM) for future Li-ion battery (LIB) applications.[1–3] This is due in part to the fact that it is isostructural with layered $LiCoO_2$—the first choice CAM since LIB commercialization—but offers higher theoretical capacities at lower costs. LNO is capable of delivering specific charge capacities >240 mAh g^{-1} at 4.3 V vs. Li^+/Li.[4] However, capacity losses of up to 20% are usually observed in the first cycle due to structural degradation for x(Li) ≤ 0.5.[5] Improved first cycle efficiencies have been achieved for LNO synthesized using excess Li,[6–8] but numerous other issues affect the cycling performance negatively, too. After several years of intense research, structural and chemical instabilities have been identified as most critical issues hindering commercialization of LNO, and battery developers started to partially substitute Ni by other metals (Mn, Co, Al), bringing NCA ($Li[Ni_{1-x-y}Co_xAl_y]O_2$) and NCM ($Li_{1+z}[Ni_{1-x-y}Co_xMn_y]_{1-z}O_2$) CAMs into the market. Such solid solution CAMs strongly benefit from synergetic effects of the different metals. However, due to increasing demands in energy density, in particular for electric vehicles, in recent years, the cathode chemistry is more and more pushed back to Ni-rich compositions (>80% Ni). This development inspired both academia and industry to revisit LNO,[9] mainly aiming at exploring the upper limit of Ni content in layered oxide CAMs.[10]

Several issues, mainly related to instabilities, are responsible for the failure of LNO cells in the past. Apart from LNO's instability under storage in air and other atmospheres,[11] its relatively low thermal stability constitutes a major problem. Partially delithiated LNO already decomposes exothermally at temperatures of 150-200 °C (note that the decomposition temperature decreases with increasing degree of delithiation).[7,12–15] Side reactions, in which cation mixing leads to formation of spinel ($LiNi_2O_4$)[12] and/or rock-salt-type phases,[7,14] were proposed as being responsible to some degree for this instability. Apart from that, instability also arises from the formation of highly reactive Ni^{IV} during charge, resulting in adverse side reactions at the electrode-electrolyte interface and formation of NiO-like surface layers. In general, it is believed that the appearance of rock-salt-type phases—sooner or later during cycling operation—causes capacity fading of Ni-rich layered CAMs, as they increase the charge transfer resistance and lower the cell reversibility/efficiency.[4,16–18]

A critical factor governing the degradation of LNO is the multistep phase transformation process occurring with Li insertion/extraction. At least four different $Li_{1-x}NiO_2$ phases have been described in the literature, namely the hexagonal H1, monoclinic M, hexagonal H2, and hexagonal H3 phases. Of note, these phases appear in the same order during Li extraction.[1,2,8,19,20] Overall, it is believed that the H2-H3 transformation at high SOC (state of charge; 4.15-4.25 V) has the strongest negative effect of all on the intrinsic stability of LNO, as it is accompanied by a sudden collapse of the structure along the crystallographic *c*-axis. Particle cracking and formation of fresh and reactive surfaces are observed when the cell voltage exceeds 4.2 V, which can be attributed to mechanical stress generated during the H2-H3 transformation.[4] Cracking already occurs within around 10 cycles and leads

to formation of additional rock-salt-type material, which in turn, increases the charge transfer resistance. Exposure of surfaces to the electrolyte typically involves side reactions with release of gas (particularly at high SOC), e.g., when electrolyte is decomposed by oxidation.[21,22] In addition, evolution of oxygen from the lattice of Ni-rich layered CAMs at high SOC has been observed.[23–25] Hence, it is necessary to examine and understand whether similar processes occur in LNO and, if so, how they contribute to degradation. In this article, we provide new insights into the structural evolution and degradation processes of LNO cells from electrochemical charge/discharge experiments, operando X-ray diffraction, and in situ pressure and gas analysis.

Results and Discussion

Scanning Electron Microscopy

Scanning electron microscopy (SEM) images of the as-prepared LNO powder are shown in Figure 1. The micrometer-sized particles are of spherical shape, and they have the typical hierarchical structure of secondary CAM particles. It can be clearly seen from the higher magnification images that these secondary particles are made of densely packed primary particles of 100-250 nm diameter, which explains the relatively small Brunauer-Emmett-Teller (BET) surface area of about 0.3 m^2 g_{LNO}^{-1} measured for this material.

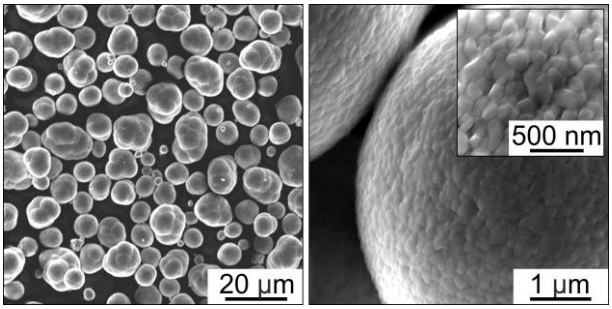

Figure 1. SEM images at different magnifications of as-prepared LNO powder.

Neutron Diffraction

As is evident from the neutron diffraction (ND) pattern shown in Figure 2, high-quality LNO, free of impurities, was obtained after calcination of the precursor mixture. The Bragg reflections can be indexed to the rhombohedral $NaFeO_2$-type structure (space-group *R*−3*m*). In the initial state, the hexagonal phase is referred to as H1 phase, with ABCABC stacking of oxygen planes, also known as O3 phase.[26] The results from Rietveld refinement analysis are summarized in Table 1. The lattice parameters are in good agreement with data reported in the literature.[27]

Because the electrochemical behavior of LNO is strongly stoichiometry-dependent,[27] the fraction of Ni in the Li layers was also determined. Due to relatively small size differences between the Ni^{II} (r = 0.69 Å) and Li^{I} ions (r = 0.76 Å),[28] Ni incorporation into the Li layers can hardly be avoided. Refinement yielded about 1% of Ni on the 3a

site. For reasons of charge neutrality, we assume nickel(II) oxidation state. Note that disorder only involves extra Ni in the Li layers, thus leading to an overall stoichiometry of $[Li_{0.99}Ni_{0.01}]_{3a}[Ni]_{3b}[O_2]_{6c}$. The fraction of Ni on Li sites is relatively low, which is also reflected in the fact that the lattice parameters closely match those of well-ordered LNO phases.[29]

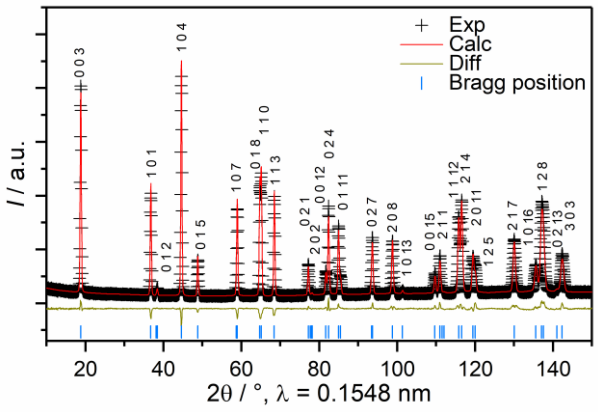

Figure 2. ND pattern of as-prepared LNO powder together with calculated and difference patterns from Rietveld refinement analysis.

Table 1. Structural parameters from Rietveld refinement analysis of ND data obtained on as-prepared LNO powder.

Phase	*x*(Li)	*a* [Å]	*c* [Å]	*c*/*a*	*V* [Å^3]
$Li_{0.99}Ni_{1.01}O_2$ (H1 phase)	0.99	2.87619(2)	14.2002(2)	4.937	101.733(2)
Atom	Site	*x*	*y*	*z*	occ
Li1	3a	0	0	0	0.993(2)
Ni1	3a	0	0	0	0.007(2)
Ni2	3b	0	0	0.5	1
O1	6c	0	0	0.24117(6)	1

Cycling Performance

LNO/Li cells were cycled in the voltage range between 3.0 and 4.3 V for 100 cycles. The first three cycles were performed at C/10 (Figure 3a). Then, the charge and discharge rates were controlled at C/4 and C/2, respectively. A Coulombic efficiency of 'only' 88.1% (q_{ch} = 249.9 mAh g_{LNO}^{-1}, q_{dis} = 220.2 mAh g_{LNO}^{-1}) was achieved in the initial cycle, which might be related to the fact that the LNO CAM employed in this work exhibits slight Li deficiency. The relation between the specific capacity of LNO and Li deficiency was reported by Rougier *et al*. for a series of $Li_{1-z}Ni_{1+z}O_2$ materials, showing an increasing irreversible capacity loss in the first cycle with increasing off-stoichiometry.[27] This result was explained by the presence of Ni^{II} in the Li layers. On

the one hand, Ni ions decrease the interslab distance due to their smaller ionic radius compared to Li^{I}, and thus, make Li diffusion more difficult. On the other hand, they are also oxidized during the charge cycle, resulting in strong electrostatic repulsion and hindering Li re-insertion. However, our cycling data indicate a regain in specific capacity during the course of the 2nd and 3rd cycles, the reason of which is not fully understood at present. At the end of the 3rd charge cycle, almost all of the Li is extracted from the LNO, leading to a composition of $Li_{0.065}NiO_2$ (Figure 3b). Note that the Li content was calculated from the specific capacity.

To identify the phase transformations occurring during cycling and understand to what extent they contribute to the measured specific capacity, closer examination of the voltage-capacity curves was carried out. The voltage profiles display the characteristic features expected for a multistep phase transformation process. The features of single phases (H1, M, H2, H3)[19] and the corresponding two-phase regions (H1-M, M-H2, H2-H3) are clearly visible in the galvanostatic trace shown in Figure 3b.

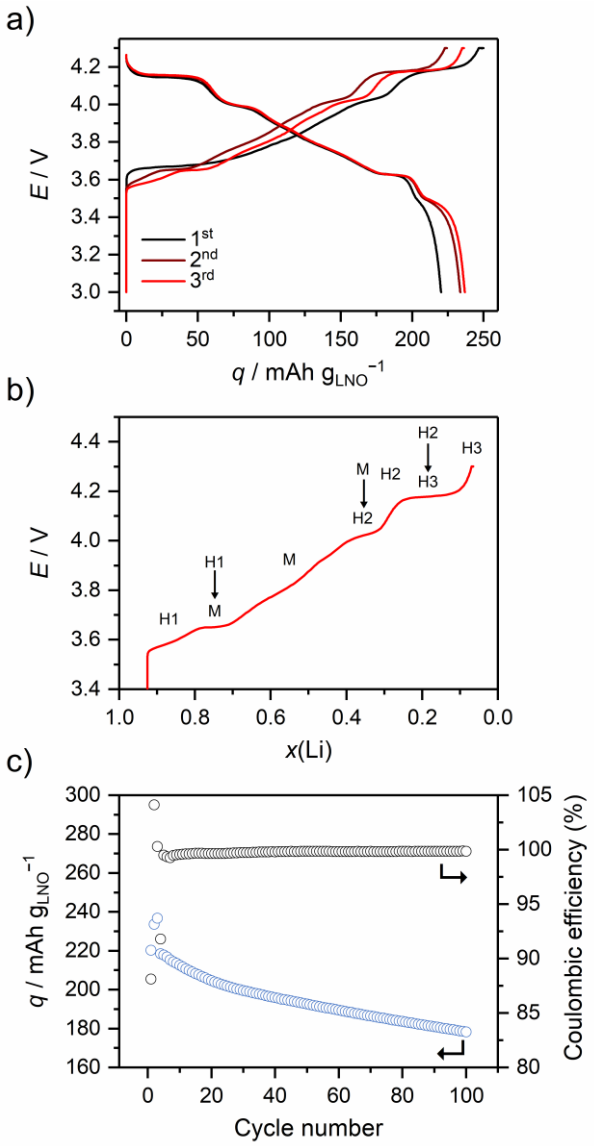

Figure 3. Cycling performance of LNO/Li cells. After the first three cycles at C/10 were completed, the charge and discharge rates were set to C/4 and C/2, respectively, in the subsequent cycles. (a) Voltage profiles for the first three cycles. (b) 3rd cycle charge trace as a function of *x*(Li). The different single- and two-phase regions are denoted. (c) Specific discharge capacity and Coulombic efficiency over 100 cycles.

The redox peaks in the differential capacity curves in Figure 4a allow clear localization and assignment of the two-phase regions, where the voltage remains virtually constant.[30] Especially the peaks corresponding to the H1-M and H2-H3 transformations [regions (I) and (III)] are relatively broad in the initial cycle. However, they become narrower in the following cycles, suggesting that these transformations are possibly kinetically hindered in the beginning of cycling. In addition to the peaks that are known to be related to the first-order H1-M, M-H2, and H2-H3 transformations,[19] the presence of some other peaks of lower intensity is also noticed. Two peaks are located in the monoclinic phase stability region at (charge)

potentials around 3.8 and 3.95 V and are denoted as M-M’ and M’-M’’, respectively [region (II)]. Thomas *et al.*[31] attributed these features to Li vacancy ordering in the Li planes, and in fact, Peres *et al*.[32] verified experimentally such ordering in monoclinic LNO by use of electron diffraction. An additional peak is seen at 3.55 V during charge and at 3.5 V during discharge in the H1 region (denoted as H1-H1’), in agreement with other studies on LNO.[1,2,5,6,8,19] Interestingly, this peak has not been observed for Ni-rich NCMs, even for compositions close to that of LNO (≥90% Ni).[33] In recent years, it has been shown that reordering of Li ions, without affecting the hexagonal symmetry, can occur for x(Li) = 8/9 (≈0.89) and 6/7 (≈0.86).[31,34] The appearance of the H1-H1’ feature in the differential capacity curves agrees well with x(Li) ≈ 0.86. Comparison of the first three cycles reveals that the capacity regain mentioned above is associated to some degree with the H1-H1’ plateau. Hence, reordering of Li ions in the almost fully lithiated LNO may be crucial for achieving high specific capacities. In fact, LNO CAMs with the largest initial discharge capacities reported in the literature apparently exhibit a pronounced H1-H1’ plateau.[4,33] However, it is also evident from the data shown in Figure 4a that the H1-H1’ peak vanishes during discharge when the C-rate is increased (here, from the 4th cycle onward). Nevertheless, the peak is still present in every charge cycle, although it becomes weaker. This finding suggests that the ordering may be kinetically limited during the (faster) discharge process, but probably occurs in the 5 min open circuit voltage (OCV) step at end of each cycle.

The specific capacity fades relatively quickly to below 80% (relative to 3rd cycle discharge capacity at C/10) after about 100 cycles (Figure 3c). A reason for the capacity degradation is certainly the buildup of (surface) resistance by particle cracking and detrimental side reactions with the electrolyte.[4] Such resistance increase contributes to polarization, shifting the oxidation and reduction peaks further apart from each other.[35] The average discharge voltage decreased by 70 mV from the 3rd to 100th cycles (Figure SI 1). Moreover, the differential capacity curves in Figure 4a show uneven polarization already during the 4th to 10th cycles. Of note, the shift in peak locations from the 3rd to 4th cycle is primarily due to the change in C-rate. Both the H1-M and H2-H3 peaks reveal significant shifts and broadening. In contrast, the peaks in the monoclinic stability region (M-M’ and M’-M’’) and the M’’-H2 peak remain at similar voltages, suggesting enhanced Li diffusivity in this range of x(Li).

Finally, the contribution of the individual single- and two-phase regions (H1, H1-M, M, M-H2, H2, H2-H3, and H3) to the capacity degradation was determined from the differential capacity curves. The loss in specific charge capacity (relative to 4th cycle at C/4) over 100 cycles is depicted in Figure 4b. During the first five cycles, a relatively strong capacity loss in the H1 region is observed. Thereafter, effectively no further losses occur in this region. In contrast, a continuous loss in capacity is seen for the H2-H3 region, while the specific capacities from the other phase transformation regions are much less affected. In addition, the capacity gained in the constant voltage (CV) step at the end of charge is also shown in Figure 4b. As expected, there is a slight increase with cycling as the overpotential increases. Yet, the total time was not sufficient to achieve equilibrium in the LNO cathode.

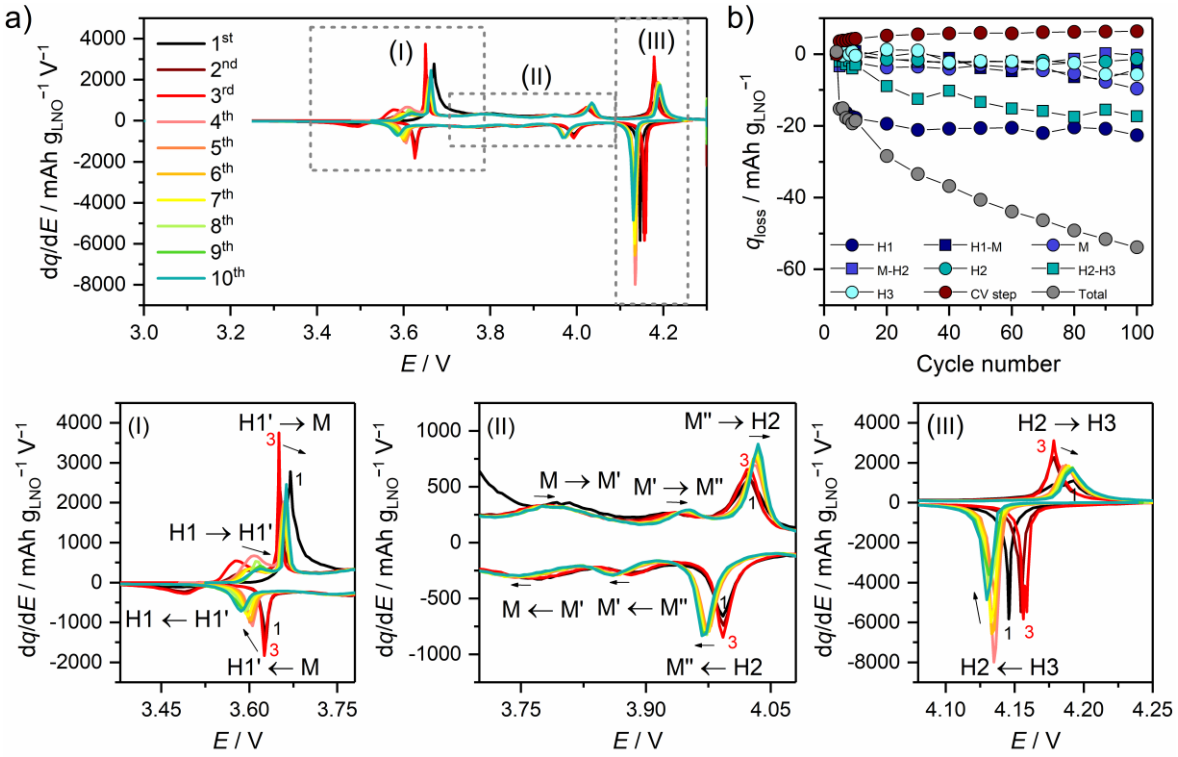

Figure 4. (a) Differential capacity plots for the first ten cycles. Dashed boxes indicate the H1-H1' and H1'-M (I), the M-M', M'-M'', and M''-H2 (II), and the H2-H3 phase transformation regions (III) magnified at the bottom. Shift in peak locations from the 3rd cycle onward is denoted by arrows. (b) Loss in specific charge capacity relative to the 4th cycle at C/4. Individual contributions from the different single- and two-phase regions and the capacity gain in the CV step at the end of charge are shown.

Differential Electrochemical Mass Spectrometry

Degradation of high-energy-density LIB cells is usually accompanied to some degree by gas evolution, and for NCMs, it has even been shown that capacity fading and gassing are closely connected processes.[21,25] Especially structural instabilities of NCM-based CAMs typically result in release of lattice oxygen.[23–25] In this work, in situ gas analysis was performed by differential electrochemical mass spectrometry (DEMS) to determine whether similar processes occur in LNO and contribute to cell degradation. Results from DEMS conducted on an LNO/Li cell are depicted in Figure 5a-c and Figure SI 2, showing the gas evolution over three cycles as a function of *x*(Li) and time, respectively. Figure 5c is a magnified view of the 3rd charge/discharge cycle. The cell was cycled at C/10 in the voltage range of 3.0-4.3 V, with OCV steps of 5 and 30 min at the end of charge and discharge, respectively. Both O_2 and CO_2 evolution is observed in each cycle, with similar and reproducible patterns of three peaks per cycle, except for O_2 in the 2nd cycle, where the first peak during charge is below the detection limit. For NCM CAMs, it has been reported that CO_2 evolution is a result of electrolyte oxidation due to oxygen release from the lattice, among others.[21,23–25,36] The first gas evolution peaks are detected in the H2 (solid solution) region during charge. Interestingly, the evolution rates reach local minima during the

H2-H3 transformation. Hence, the phase transformation seems to stabilize the lattice structure, which is somewhat surprising at first glance. However, in the single-phase H3 region, both the O_2 and CO_2 evolution rates increase again sharply, with maxima at the cut-off potential. This result suggests that the H3 phase is not stable enough to prevent oxygen release from the LNO lattice. As expected, the evolution rates decrease during discharge, reaching again local minima in the H3-H2 transformation region. Similar (symmetric) to the 1st peak on charge, a 3rd peak is detected in the H2 region. This means that O_2 evolution is observed very clearly not only during charge, but also discharge, which, to our knowledge, has been reported so far only for Ni-rich NCM in an all-solid-state battery cell configuration.[37] No further O_2 evolution is detected during formation of the monoclinic phase, thus suggesting a stable lattice structure. The shape of the O_2 evolution peaks remains more or less the same for all cycles, but the relative height ratio of the 2nd and 3rd peak varies (Figure SI 2). In the initial cycle, the peak during discharge is larger than that at the end of charge. For the 2nd and 3rd cycles, it is vice versa. In Figure 5a, the O_2 peak in the H2 phase appears at slightly lower potential compared to the CO_2 peak, the reason of which is unclear, also because the peak locations (maxima) match for O_2 and CO_2 in the H3 phase and the H2 phase during discharge. The gas evolution in the H2 phase reaches its maximum at x(Li) ≈ 0.3 and is slightly shifted in the initial cycle. O_2 evolution in the H3 phase begins for x(Li) < 0.2, which is in agreement with findings for different NCM CAMs.[23,25] For example, Jung *et al*. reported an SOC of about 81% as the onset of O_2 evolution in NCM622 (60% Ni) cells.[23] Note that the initial increase in O_2 and CO_2 evolution rates in Figure 5b is because the gassing during OCV (prior to discharge) is included in these data. Because no charge is transferred, x(Li) remains constant while the evolution rates vary. Nevertheless, they drop sharply with discharge.

The total amounts of evolved O_2 and CO_2 were determined to be 8 µmol g_{LNO}^{-1} and 27 µmol g_{LNO}^{-1}, respectively (Figure SI 2). Assuming that the oxygen release in the delithiated state of LNO leads to formation of NiO according to $Li_0NiO_2 \rightarrow NiO + 1/2\ O_2$, a 1.1 nm-thick NiO surface shell should have formed. When additionally assuming that the detected CO_2 only stems from the reaction of lattice oxygen with the electrolyte, the layer thickness would increase to 4.7 nm. These findings are in accordance with TEM studies by Yoon *et al*., who observed the formation of a NiO-like phase (space-group *Fm*−3*m*) at the top surface of LNO particles cycled to 4.1 V in half-cells with a Li metal anode for 100 cycles.[4] The thickness of the surface layer was around 20 nm. Figure SI 3 shows results from a DEMS measurement on $LiNi_{0.85}Co_{0.1}Mn_{0.05}O_2$ (NCM851005). Interestingly, O_2 evolution can be clearly observed at the end of charge and during discharge after the plateau at high voltage. In summary, in addition to LNO, also NCM with a high Ni content shows oxygen release during discharge (in LIB cells), however, to a much lower degree. Apparently, O_2 evolution is correlated with structural arrangements in the CAM. However, it should be noted that there is an ongoing discussion in the literature about the contribution of oxygen (or anion) redox to the total capacity. According to Seo *et al*.,[38] oxygen redox activity can be expected for overlithiated and disordered cathode materials with Li-O-Li bond configuration (rather than only Li-O-TM). In the case of

ordered layered oxide CAMs, this type of bonding is scarce, i.e., Ni is primarily oxidized during charge.[39]

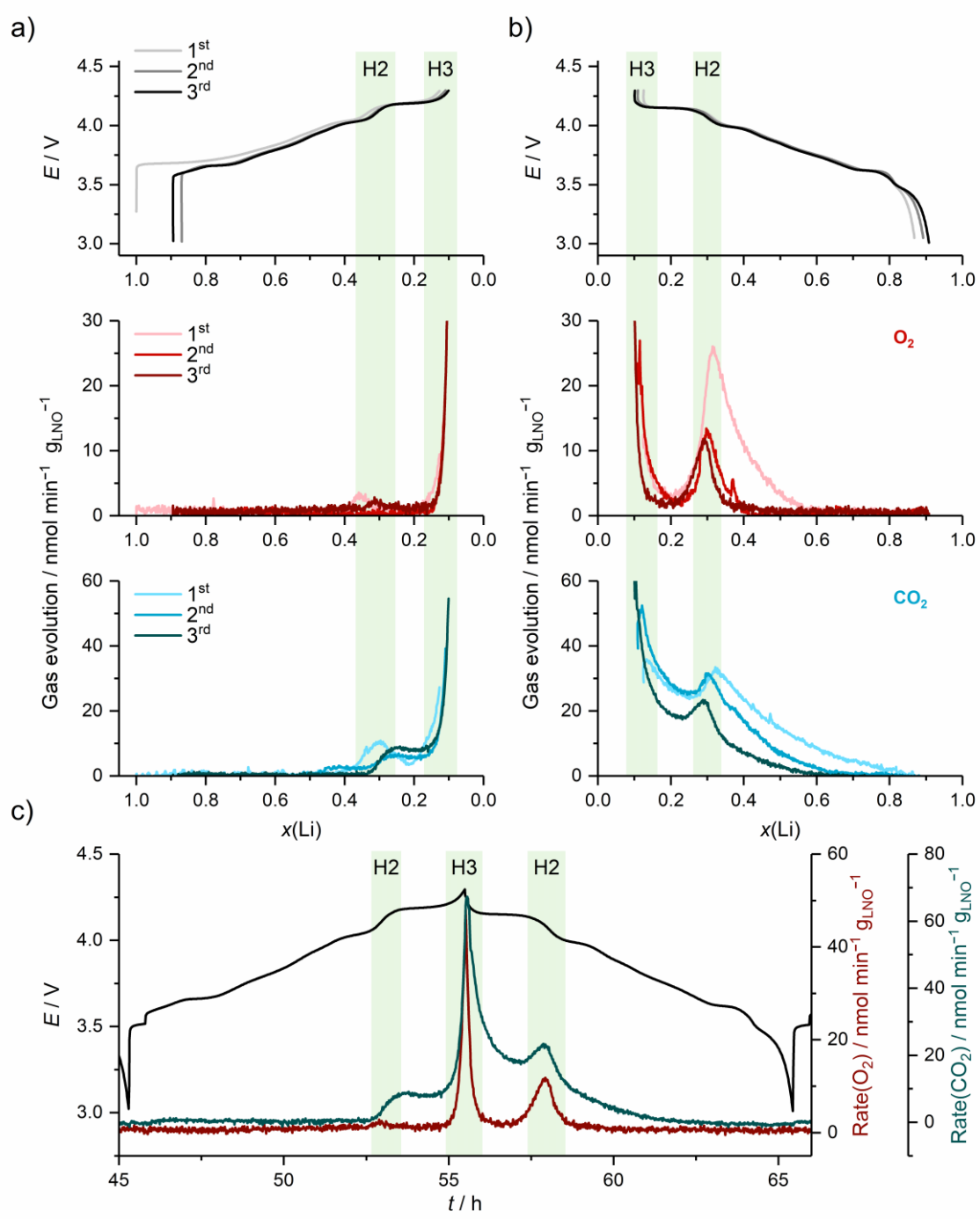

Figure 5. (a) Charge and discharge curves (b) and the corresponding evolution rates of O_2 and CO_2 as a function of *x*(Li) during DEMS measurement on an LNO/Li cell cycled at C/10. H2 and H3 phase regions are highlighted in green. (c) Magnified view of the 3rd cycle.

X-ray Diffraction

Structural changes of LNO with de-/lithiation were studied by operando X-ray diffraction (XRD). In the past, some operando diffraction data sets on LNO have been reported,[1,19,33] but mostly with low time resolution. Besides, they only provide an approximate overview of phase regions in the phase diagram of Li_xNiO_2. An updated version of structural data on LNO was recently reported by Li *et al*.[40] However, the resolution (in terms of *x*(Li)) is still not sufficient to draw unequivocal conclusions about the interconnection of structural changes and the observed gas formation. In this work, XRD was performed on LNO/Li cells using a laboratory diffractometer optimized for battery research,[41] allowing high-quality data of good time resolution to be collected. Hence, better identification of the two-phase regions and direct correlation of structural changes with cell potential are ensured. Because the 1st cycle electrochemistry differs to some degree from the subsequent cycles, the diffraction data obtained in the 2nd cycle were examined in more detail.

A contour plot showing the evolution of Bragg reflections as a function of cell potential is presented in Figure 6a. The presence of single-phase and coexisting phase regions, as indicated by the different slopes in the voltage profile on the right hand side of the figure, agrees well with the expected changes in Bragg reflections. In the H1, M, H2 and H3 phase regions, the reflections shift to varying degrees, and clear peak splitting is noticed during both the monoclinic distortion and the H2-H3 transformation (Figure 6b).

The crystallographic changes during charging were evaluated by Rietveld refinement analysis (Figure 7a-d). The lattice parameters, the unit cell volume, the relative weight fractions, and the oxygen *z* position of all phases were considered in the refinement (for the monoclinic phase, the oxygen *x* position was also determined). The conversion of monoclinic to hexagonal lattice parameters was accomplished according to $a_{\mathrm{h}} = \left(a_{\mathrm{m}}/\sqrt{3} + b_{\mathrm{m}}\right)/2$ and $c_{\mathrm{h}} = 3c_{\mathrm{m}}\sin(\beta)$.[1]

The two-phase regions are located at 0.80 ≥ *x*(Li) ≥ 0.75 for H1-M, 0.40 ≥ *x*(Li) ≥ 0.36 for M-H2, and 0.26 ≥ *x*(Li) ≥ 0.16 for H2-H3. Note that individual phases were only taken into account in the Rietveld analysis when their relative weight fraction exceeded 20%. Unlike all other phase transformations, the H2-H3 region is found to extend over a relatively wide range of *x*(Li). This indicates a broader miscibility gap, which is also reflected in the presence of a distinct voltage plateau. $Li_{0.26}NiO_2$ and $Li_{0.16}NiO_2$ can be defined as thermodynamically stable single-phase end members of the H2-H3 transformation.

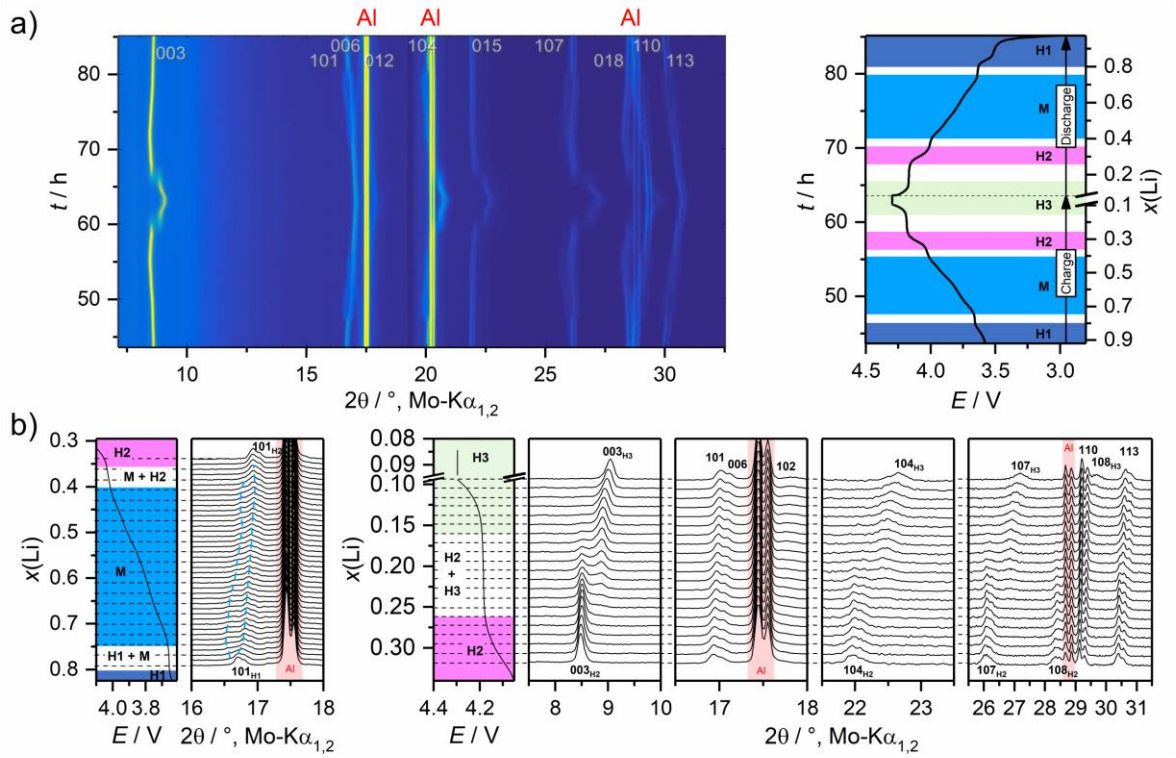

Figure 6. Operando XRD of an LNO/Li cell at C/20 in the 2nd cycle. (a) Contour plot showing the evolution of Bragg reflections and the corresponding voltage profile as a function of *x*(Li) and measurement time. The different single-phase regions are highlighted for clarity. (b) Selected diffraction patterns showing the splitting of 101 reflection in the monoclinic phase region and selected diffraction patterns of the H2-H3 transformation region.

Hexagonal H1 Phase Region

Upon charging, the *a*-lattice parameter decreases while *c* increases. This behavior is well known for LNO and isostructural NCM- and NCA-based CAMs and can be attributed to the combined effect of transition metal oxidation, leading to increasing oxygen repulsion along the *c*-axis due to the decreasing screening effect of Li ions, among others.[42,43] Overall, the XRD data can be described by a single H1 phase up to a charge potential of 3.65 V and Li content of 0.80. The presence of the additional H1-H1' peak around 3.55 V [region (I) in Figure 4a] is not reflected in the patterns in terms of e.g., splitting of reflections or changes in FWHM intensities. Consequently, it is reasonable to assume that the H1 phase is the only stable phase in this range of *x*(Li), showing solid solution behavior, in agreement with previous studies.[1,5,8,19] Li ordering is believed to be responsible for the changes in slope of the voltage profile. For the layered intercalation compound Li_xTiS_2, it has been demonstrated that Li ordering may be a factor governing the changes seen in the corresponding differential capacity curves.[34,44] When Li ions are mobile at room temperature, they can form arrays without distinct phase boundaries, controlled by Li^+-Li^+ interactions due to long-range Coulomb repulsion. Such superstructure formation can directly

affect the thermodynamics and electrochemical characteristics but is not necessarily detectable via XRD because of the relatively small scattering cross-section of Li.

Monoclinic M Phase Region

The monoclinic structure is observed for x(Li) ≤ 0.80. In contrast, Ohzuku *et al.*[1] reported 1 ≥ x(Li) ≥ 0.7 for the H1 solid solution region, but the XRD experiments were only performed for few different SOCs. Other groups reported x(Li) = 0.85 and 0.79 as the onset of monoclinic distortion, which is in agreement with our results.[19,40] Of note, the monoclinic phase is already visible in the XRD patterns at slightly higher degrees of lithiation (it is only considered when its relative weight fraction is ≥20%, as mentioned above). In the two-phase region, the lattice parameters of both the H1 and M phases remain fairly constant.

In the solid solution region (0.75 ≥ x(Li) ≥ 0.40), variations in monoclinic peak splitting are observed, which correlate with the changes in cell potential (see 101 reflection in Figure 6b). When the potential exceeds about 3.69 V, initial splitting into the monoclinic 20−1 and 111 reflections is noticed. Then, the reflections converge and have a minimum discrepancy around 3.87 V. At about 3.9 V, the splitting widens again until the end of the monoclinic phase stability region and the M-H2 transformation occurs. The two regions of pronounced splitting can be associated with the additional peaks at 3.8 (M-M') and 3.95 V (M'-M'') in the differential capacity curves [region (II) in Figure 4a]. It is believed that a cooperative Jahn-Teller effect due to presence of Jahn-Teller active Ni^{III} ions is the reason for the monoclinic distortion.[1,45] However, Peres *et al*. proposed Li vacancy ordering as an alternative explanation, leading to formation of a monoclinic superstructure.[32] Using electron diffraction, they observed a cell four times larger than the monoclinic one determined previously by X-ray and neutron diffraction.[1,8,19,45,46] Unlike other studies available in the literature, Yang *et al*. found a first-order phase transition in the range 0.75 > x(Li) > 0.45, but assigned the sets of peaks to two hexagonal phases.[47] Our results do not confirm this hypothesis. The observed shift of split reflections in the patterns is clearly not in accordance with the thermodynamics of a conventional two-phase transformation model, where the reflections of both phases remain at fixed 2θ positions until the reaction is completed. We therefore consider the monoclinic structure as proven. A description of diffraction patterns by a single-phase model is possible, in general, when considering Li vacancy ordering, as suggested by Peres *et al*., as the cause for both the additional features in the voltage profile and the observed changes in the magnitude of monoclinic distortion.[32]

Hexagonal H2 Phase Region

The presence of distinct (individual) Bragg reflections, as shown in Figure 6b, evidences the back-transformation of the monoclinic structure into the hexagonal H2 structure for x(Li) ≤ 0.40 (4.02 V). Once the two-phase region is passed, the c-lattice parameter begins to decrease while a continues to decrease slightly. Note that x(Li) = 0.36 is identified here as the onset of c-lattice parameter contraction.

Hexagonal H3 Phase Region

The contraction along the *c*-axis becomes significantly stronger when the H2 phase transforms into the H3 phase, which is often referred to as collapse of the layered crystalline structure.[48] The H3 phase is detected for the first time when x(Li) = 0.26. Because of the strong mismatch in *c*-lattice parameter between the H2 and H3 phases, the presence of H3 is clearly apparent in the diffraction patterns (Figure 6b). At the end of charge, x(Li) = 0.08 is achieved and the *a*- and *c*-lattice parameters are 2.815(3) Å and 13.506(2) Å, corresponding to a relative decrease by 2.1% and 5.0%, respectively, compared to initial state (prior to charge).

The unit cell volume decreases continuously during delithiation (Figure 7b). The relative change from the beginning to the end of charge was determined to be 9.0%, but most of the volume shrinkage (6.0%) occurs for x(Li) ≤ 0.26, of which 3.8% can be attributed to the H2-H3 transformation. Overall, our results are in good agreement with structural data published by Yoon *et al*.[33] The same largely holds true for data reported by Li *et al*.[40] except that, similar to Li *et al*.[19] and Arai *et al*.[8], the presence of a single H3 phase at the end of charge has not been observed.

In summary, the changes in crystallographic *c*-axis are the result of changes in the Li-O and Ni-O bond distances, which were calculated from the refinement of oxygen *z*-position (Figure 7d). Note that due to the lower scattering power of oxygen, the refinement is more error prone, with the data points exhibiting larger scatter. Nevertheless, Li-O and Ni-O show opposite trends with decreasing x(Li). A similar behavior as for NCM811 is found,[48] where the Ni-O distance decreases and the Li-O distance increases at first. The LNO results clearly show that the Li-O distance begins to decline slowly for x(Li) ≤ 0.26 and collapses for x(Li) ≤ 0.14. Interestingly, this means that the sharp shrinkage of the Li layer (reflected in the Li-O distance) does not occur during the H2-H3 transformation but when the two-phase transformation is finished and the H3 phase further delithiated. This result is in line with the findings from gas analysis, where the maximum evolution rates are not observed during the H2-H3 transformation. It is believed that the severe shrinkage of the interslab space in layered oxide CAMs is, in part, related to changes in electronic structure, i.e., modification of the O and Ni (or, in general, transition metal) binding orbitals. Soft X-ray absorption spectroscopy studies on both delithiated LNO and NCM811 have shown that the holes, compensating the Li extraction, are primarily located in the O 2p states rather than in the Ni 3d states, thus leading to large mixing of O 2p and partially filled Ni e_g orbitals.[48,49] Density functional theory calculations suggest that this mixing results in depletion of the oxygen charge, causing the collapse of the layered structure. Moreover, it has been shown that the surface electronic structure of $Li_{1-x}NiO_2$ is different from the bulk and that initially Ni^{II} at the top surface is mostly oxidized to Ni^{III} during Li extraction, whereas in the bulk, Ni ions are oxidized from Ni^{III} to Ni^{IV}.[50] It is believed that partial transfer of e^- from the 2p band results in oxidation of the oxygen anions.[51] Hence, when LNO is charged to high potentials, nickel is oxidized to Ni^{IV} and gas may be released due to reactions with the O 2p band.

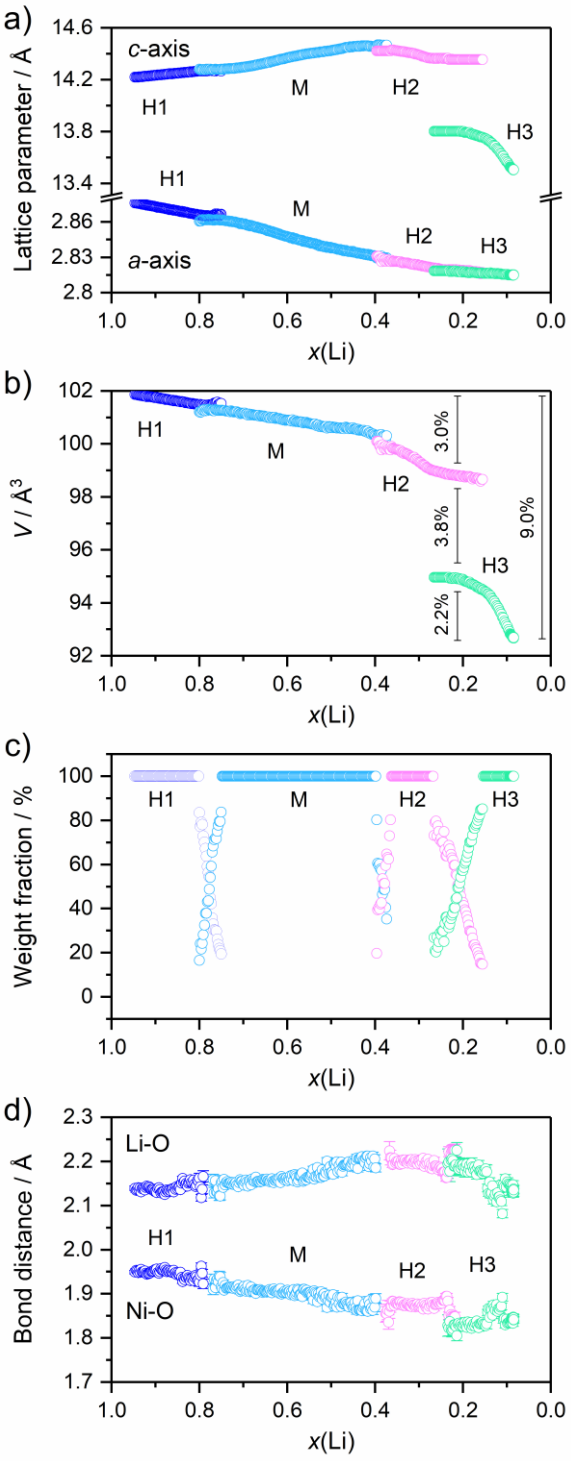

Figure 7. Results from Rietveld refinement analysis of operando XRD data obtained on an LNO/Li cell. (a) Evolution of *a*- and *c*-lattice parameters, (b) unit cell volume, (c) weight fractions, and (d) Li-O and Ni-O bond distances for the different Li_xNiO_2 phases in the 2nd charge cycle.

Pressure Analysis

The LNO volume changes with cycling were also analyzed on an electrode level by in situ pressure measurements. This method has already been used to monitor Li

plating/stripping and the volume expansion/contraction of graphite and silicon anodes.[52–54] A detailed description of the setup used and the general working principle can be found in refs.[52,54] as well as in Appendix SI 1 and Figure SI 4.

The measured volume changes of an LNO/$Li_4Ti_5O_{12}$ (LTO) cell together with the LNO potential vs. Li reference (three-electrode configuration) are depicted in Figure 8a. LTO was used as the counter electrode, as it exhibits negligible volume changes upon cycling.[55] The LNO/LTO cell was cycled at C/5 in the voltage range of 1.45-2.8 V, corresponding to cut-off potentials of about 3.0 and 4.3 V with respect to Li^+/Li. The maximum volume change was around 9%. As expected, the smallest overall volume or largest contraction is observed at the upper cut-off potential when the majority of Li is removed from the LNO lattice. Although the measurement has a limited resolution, the most pronounced changes are clearly seen during the H2-H3 transformation. In Figure 8b, the relative volume changes as a function of LNO potential from in situ pressure measurement are compared to the operando XRD results. In the latter case, the volume changes were calculated based on the unit cell volume of the different phases and their relative weight fractions. As is evident, the data sets from both techniques match quite well and reveal the largest contraction during the H2-H3 transformation at about 4.2 V. The potential-dependent discrepancy in ΔV between the in situ pressure and operando XRD measurements can be explained, among others, by the fact that gas evolution during cycling operation somewhat interferes with the measured pressure changes, leading to slightly different curve shapes. It should be noted, nevertheless, that the specific charge capacities achieved in the XRD (≈235 mAh g_{LNO}^{-1}; 2nd cycle) and pressure measurements (≈205 mAh g_{LNO}^{-1}; 18th cycle) vary to some degree. Because the largest changes occur during the H2-H3 transformation, the region at high SOC is mainly responsible for the total volume contraction. As mentioned above, Li is irreversibly consumed upon cycling, thus leading to lower specific capacities, but still, a high SOC (including the H2-H3 transformation) can be reached at the end of charge in the later cycles. Consequently, it is reasonable that both experiments indicate similar overall volume changes despite differences in specific capacity.

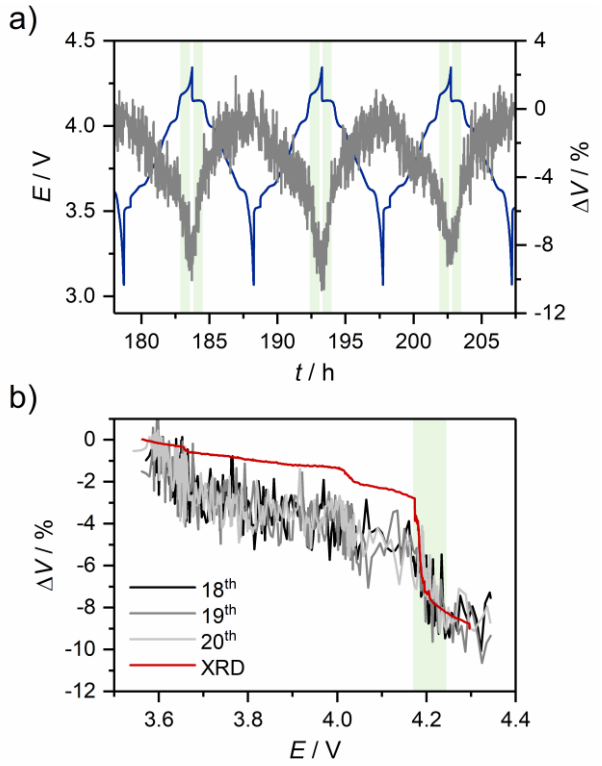

Figure 8. In situ pressure analysis of an LNO/LTO cell cycled at C/5. (a) LNO potential vs. Li reference electrode (blue) and the corresponding volume changes of LNO (gray). (b) Comparison of volume changes during charging from XRD (red line) and in situ pressure measurement. The H2-H3 phase transformation region is highlighted in green.

Conclusions

The phase transformations occurring in LNO during cycling in the voltage range between 3.0 and 4.3 V vs. Li^+/Li and their effect on the overall stability of this high-capacity cathode active material were analyzed by a combination of galvanostatic charge/discharge experiments, operando X-ray diffraction, and in situ pressure and gas analysis. For x(Li) ≥ 0.26, moderate changes in crystal structure from the initial hexagonal H1—via monoclinic distortion—to the hexagonal H2 phase were accompanied by formation of several superstructures, one in the H1 and two in the M phase stability region, probably as a result of Li vacancy ordering. For x(Li) ≤ 0.26, the LNO lattice underwent severe changes with a sudden collapse of the crystallographic *c*-axis, resulting in a volume contraction of 3.8% (out of 9.0% in total) upon H2-H3 transformation. The volume contraction and expansion with charging and discharging, respectively, were not only measurable on the atomic length scale via X-ray diffraction, but also on the electrode level via pressure analysis. Interestingly, the largest decrease in Li-interslab space, reflected in the Li-O bond distance, did not occur during the H2-H3 transformation, but rather when it was completed and the H3 phase further delithiated (x(Li) ≤ 0.16). Gas analysis via differential electrochemical mass spectrometry revealed that oxygen release from the LNO lattice takes place in the H2 and H3 solid solution regions and is largely

suppressed during the H2-H3 transformation, thus providing new insights into the relationship between structural changes and lattice instabilities. In summary, apart from the H2-H3 transformation, there is at least one other factor controlling the lattice stability, and thus, ultimately also the longevity of LNO cells.

Experimental Section

For solid-state synthesis of LNO, proper amounts of $Ni(OH)_2$ (BASF SE) and $LiOH{\cdot}H_2O$ (Sigma Aldrich) precursors were mixed (1.01:1 Li/Ni molar ratio), then heated in O_2 at 15 L h^{-1} and calcined at 700 °C for 6 h. The heating and cooling rates were set to 3 K min^{-1}. The obtained LNO CAM powder was stored under Ar atmosphere.

Cathodes were prepared by slurry casting onto Al foil. The slurry was obtained by dispersing 94 wt.% LNO, 1 wt.% Super C65 carbon black (Timcal), 2 wt.% SFG6L graphite (Timcal), and 3 wt.% Solef polyvinylidene fluoride binder (Solvay) in N-ethyl-2-pyrrolidone.

For electrochemical testing, coin cells with LNO cathode (8.9 mg_{LNO} cm^{-2}), GF/D glass microfiber separator (GE Healthcare Life Sciences, Whatman), and Li metal anode (Albemarle Germany GmbH) of diameters 13, 17, and 13 mm, respectively, using LP57 electrolyte (1M $LiPF_6$ in 3:7 by weight ethylene carbonate and ethyl methyl carbonate; BASF SE) were assembled inside an Ar-filled glove box. Cycling was performed at 25 °C in the voltage range between 3.0 and 4.3 V in constant current/constant voltage (CCCV) mode. In the first three cycles, the C-rate was set to C/10 (1C = 225 mA g_{LNO}^{-1}, i = 2 mA cm^{-2}), and a CV step was applied at 4.3 V for 15 min or until the current dropped to C/20. Subsequently, the cells were cycled at charge and discharge rates of C/4 and C/2, respectively, and with a CV step at 4.3 V for 10 min or until the current dropped to C/20. In addition, a 5 min resting period under open circuit voltage conditions was applied at the end of both charge and discharge in all cycles.

For in situ gas analysis, differential electrochemical mass spectrometry (DEMS) was utilized. DEMS cells had two connections (gas in- and outlets), with a special design of the upper current collector. Details are provided elsewhere.[56,57] During the measurement, a constant carrier gas flow (2.5 mL_{He} min^{-1}, purity 6.0) was used for proper gas extraction, and the evolved gases were analyzed by a mass spectrometer (GSD 320, OmniStar Gas Analysis System, Pfeiffer Vacuum GmbH). LNO (30 mm diameter with 4 mm hole for gas extraction, 8.9 mg_{LNO} cm^{-2}), GF/D (36 mm diameter), Li metal (35 mm diameter), and LP57 were used as cathode, separator, anode, and electrolyte, respectively.

For structural characterization of as-prepared LNO, neutron diffraction (ND) was conducted on the powder material. ND data were collected at λ = 1.5482 nm using the high-resolution powder diffractometer SPODI, MLZ Garching. The measurement was performed in an airtight vanadium container. Changes in crystal structure upon cycling were followed by operando X-ray diffraction (XRD). To this end, pouch cells

with LNO cathode (20 × 40 mm^2, 10.9 mg_{LNO} cm^{-2}), Celgard 2500 polypropylene separator (30 × 50 mm^2), Li metal anode (24 × 44 mm^2), and LP57 electrolyte were assembled inside a dry room (dew point < −50 °C). During galvanostatic charging and discharging at C/20 in the voltage range of 3.0-4.3 V, diffraction data were recorded using a laboratory diffractometer optimized for battery research.[41] Patterns were acquired with a time resolution of 180 s, and they were evaluated by Rietveld refinement analysis. Refinement of both ND and XRD data was performed using the software TOPAS-Academic V5.

For analysis of volume changes on an electrode level, the pressure evolution in (constant-volume) custom cells during cycling was monitored in situ, as described elsewhere.[21,52,54] Pressure sensors (PAA33X-V-3, Omega) were connected to cells with LNO cathode (40 mm diameter with 4 mm hole for gas extraction, 5.8 mg_{LNO} cm^{-2}), GF/A separator (40 mm diameter), $Li_4Ti_5O_{12}$ anode (40 mm diameter with 4 mm hole for Li metal reference electrode, 13.8 mg_{LNO} cm^{-2}), and LP57 electrolyte. The cells for both DEMS and pressure measurements were assembled inside an Ar-filled glove box (MBraun).

Scanning electron microscopy was performed at 10 keV on a LEO-1530 electron microscope (Carl Zeiss AG).

Acknowledgements

This study is part of the projects being funded within the BASF International Network for Batteries and Electrochemistry. We thank Dr. Markus Hölzel and Dr. Volodymyr Baran for the neutron diffraction experiments performed at the SPODI instrument at the Heinz Maier-Leibnitz Zentrum (MLZ), Garching, Germany. We thank Holger Geßwein and Reiner Mönig for provision of the operando XRD instrument and their technical support.

Conflict of interest

The authors declare no conflict of interest.

References

[1] T. Ohzuku, A. Ueda, M. Nagayama, *J. Electrochem. Soc.* **1993**, *140*, 1862-1870.

[2] W. Ebner, D. Fouchard, L. Xie, *Solid State Ion.* **1994**, *69*, 238-256.

[3] J. M. Tarascon, G. Vaughan, Y. Chabre, L. Seguin, M. Anne, P. Strobel, G. Amatucci, *J. Solid State Chem.* **1999**, *147*, 410-420.

[4] C. S. Yoon, D.-W. Jun, S.-T. Myung, Y.-K. Sun, *ACS Energy Lett.* **2017**, *2*, 1150-1155.

[5] H. Arai, S. Okada, Y. Sakurai, J. Yamaki, *Solid State Ion.* **1997**, *95*, 275-282.

[6] H. Arai, S. Okada, Y. Sakurai, J. Yamaki, *J. Electrochem. Soc.* **1997**, *144*, 3117-3125.

[7] H. Arai, S. Okada, Y. Sakurai, J. Yamaki, *Solid State Ion.* **1998**, *109*, 295-302.

[8] H. Arai, S. Okada, H. Ohtsuka, M. Ichimura, J. Yamaki, *Solid State Ion.* **1995**, *80*, 261-269.

[9] M. Bianchini, M. Roca-Ayats, P. Hartmann, T. Brezesinski, J. Janek, *Angew. Chem.* 10.1002/ange.201812472; *Angew. Chem. Int. Ed.* 10.1002/anie.201812472.

[10] L. de Biasi, A. O. Kondrakov, H. Geßwein, T. Brezesinski, P. Hartmann, J. Janek, *J. Phys. Chem. C* **2017**, *121*, 26163-26171.

[11] H. S. Liu, Z. R. Zhang, Z. L. Gong, Y. Yang, *Electrochem. Solid-State Lett.* **2004**, *7*, A190-A193.

[12] J. R. Dahn, E. W. Fuller, M. Obrovac, U. von Sacken, *Solid State Ion.* **1994**, *69*, 265-270.

[13] Z. Zhang, D. Fouchard, J. R. Rea, *J. Power Sources* **1998**, *70*, 16-20.

[14] H. Arai, M. Tsuda, K. Saito, M. Hayashi, K. Takei, Y. Sakurai, *J. Solid State Chem.* **2002**, *163*, 340-349.

[15] H. Arai, M. Tsuda, Y. Sakurai, *J. Power Sources* **2000**, *90*, 76-81.

[16] D. P. Abraham, R. D. Twesten, M. Balasubramanian, I. Petrov, J. McBreen, K. Amine, *Electrochem. Commun.* **2002**, *4*, 620-625.

[17] S. Watanabe, M. Kinoshita, T. Hosokawa, K. Morigaki, K. Nakura, *J. Power Sources* **2014**, *260*, 50-56.

[18] S. Zheng, R. Huang, Y. Makimura, Y. Ukyo, C. A. Fisher, T. Hirayama, Y. Ikuhara, *J. Electrochem. Soc.* **2011**, *158*, A357-A362.

[19] W. Li, J. N. Reimers, J. R. Dahn, *Solid State Ion.* **1993**, *67*, 123-130.

[20] A. Hirano, R. Kanno, Y. Kawamoto, Y. Takeda, K. Yamaura, M. Takano, K. Ohyama, M. Ohashi, Y. Yamaguchi, *Solid State Ion.* **1995**, *78*, 123-131.

[21] B. B. Berkes, A. Schiele, H. Sommer, T. Brezesinski, J. Janek, *J. Solid State Electrochem.* **2016**, *20*, 2961-2967.

[22] H. Wang, E. Rus, T. Sakuraba, J. Kikuchi, Y. Kiya, H. D. Abruña, *Anal. Chem.* **2014**, *86*, 6197-6201.

[23] R. Jung, P. Strobl, F. Maglia, C. Stinner, H. A. Gasteiger, *J. Electrochem. Soc.* **2018**, *165*, A2869-A2879.

[24] R. Jung, M. Metzger, F. Maglia, C. Stinner, H. A. Gasteiger, *J. Phys. Chem. Lett.* **2017**, *8*, 4820-4825.

[25] R. Jung, M. Metzger, F. Maglia, C. Stinner, H. A. Gasteiger, *J. Electrochem. Soc.* **2017**, *164*, A1361-A1377.

[26] C. Delmas, C. Fouassier, P. Hagenmuller, *Physica* **1980**, *99B*, 81-85.

[27] A. Rougier, P. Gravereau, C. Delmas, *J. Electrochem. Soc.* **1996**, *143*, 1168-1175.

[28] R. D. Shannon, *Acta Crystallogr., Sect. A: Cryst. Phys., Diffr., Theor. Gen. Crystallogr.* **1976**, *32*, 751-767.

[29] J. R. Dahn, U. von Sacken, C. A. Michal, *Solid State Ion.* **1990**, *44*, 87-97.

[30] C. Liu, Z. G. Neale, G. Cao, *Mater. Today* **2016**, *19*, 109-123.

[31] M. G. S. R. Thomas, W. I. F. David, J. B. Goodenough, P. Groves, *Mater. Res. Bull.* **1985**, *20*, 1137-1146.

[32] J. P. Peres, F. Weill, C. Delmas, *Solid State Ion.* **1999**, *116*, 19-27.

[33] C. S. Yoon, H.-H. Ryu, G.-T. Park, J.-H. Kim, K.-H. Kim, Y.-K. Sun, *J. Mater. Chem. A* **2018**, *6*, 4126-4132.

[34] A. H. Thompson, *Phys. Rev. Lett.* **1978**, *40*, 1511-1514.

[35] J. B. Goodenough, K.-S. Park, *J. Am. Chem. Soc.* **2013**, *135*, 1167-1176.

[36] T. Hatsukade, A. Schiele, P. Hartmann, T. Brezesinski, J. Janek, *ACS Appl. Mater. Interfaces* **2018**, *10*, 38892-38899.

[37] T. Bartsch, F. Strauss, T. Hatsukade, A. Schiele, A-Y. Kim, P. Hartmann, J. Janek, T. Brezesinski, *ACS Energy Lett.* **2018**, *3*, 2539-2543.

[38] D.-H. Seo, J. Lee, A. Urban, R. Malik, S. Kang, G. Ceder, *Nat. Chem.* **2016**, *8*, 692-697.

[39] A. N. Mansour, X. Q. Yang, X. Sun, J. McBreen, L. Croguennec, C. Delmas, *J. Electrochem. Soc.* **2000**, *147*, 2104-2109.

[40] H. Li, N. Zhang, J. Li, J. R. Dahn, *J. Electrochem. Soc.* **2018**, *165*, A2985-A1993.

[41] L. de Biasi, G. Lieser, J. Rana, S. Indris, C. Dräger, S. Glatthaar, R. Mönig, H. Ehrenberg, G. Schumacher, J. R. Binder, H. Geßwein, *CrystEngComm* **2015**, *17*, 6163-6174.

[42] X. Zhang, A. Mauger, Q. Lu, H. Groult, L. Perrigaud, F. Gendron, C. M. Julien, *Electrochim. Acta* **2010**, *55*, 6440-6449.

[43] A. Van der Ven, M. K. Aydinol, G. Ceder, G. Kresse, J. Hafner, *Phys. Rev. B* **1998**, *58*, 2975-2987.

[44] A. J. Berlinsky, W. G. Unruh, W. R. McKinnon, R. R. Haering, *Solid State Commun.* **1979**, *31*, 135-138.

[45] A. Hirano, R. Kanno, Y. Kawamoto, K. Oikawa, T. Kamiyama, F. Izumi, *Solid State Ion.* **1996**, *86*, 791-796.

[46] R. Kanno, H. Kubo, Y. Kawamoto, T. Kamiyama, F. Izumi, Y. Takeda, M. Takano, *J. Solid State Chem.* **1994**, *110*, 216-225.

[47] X. Q. Yang, X. Sun, J. McBreen, *Electrochem. Commun.* **1999**, *1*, 227-232.

[48] A. O. Kondrakov, H. Geßwein, K. Galdina, L. de Biasi, V. Meded, E. O. Filatova, G. Schumacher, W. Wenzel, P. Hartmann, T. Brezesinski, J. Janek, *J. Phys. Chem. C* **2017**, *121*, 24381-24388.

[49] Y. Uchimoto, H. Sawada, T. Yao, *J. Power Sources* **2001**, *97-98*, 326-327.

[50] W.-S. Yoon, K. Y. Chung, J. McBreen, D. A. Fischer, X.-Q. Yang, *J. Power Sources* **2006**, *163*, 234-237.

[51] R. Hausbrand, G. Cherkashinin, H. Ehrenberg, M. Gröting, K. Albe, C. Hess, W. Jaegermann, *Mater. Sci. Eng. B* **2015**, *192*, 3-25.

[52] S. Schweidler, L. de Biasi, A. Schiele, P. Hartmann, T. Brezesinski, J. Janek, *J. Phys. Chem. C* **2018**, *122*, 8829-8835.

[53] A. Schiele, B. Breitung, A. Mazilkin, S. Schweidler, J. Janek, S. Gumbel, S. Fleischmann, E. Burakowska-Meise, H. Sommer, T. Brezesinski, *ACS Omega* **2018**, *3*, 16706-16713.

[54] A. Schiele, T. Hatsukade, B. B. Berkes, P. Hartmann, T. Brezesinski, J. Janek, *Anal. Chem.* **2017**, *89*, 8122-8128.

[55] T. Ohzuku, A. Ueda, N. Yamamoto, *J. Electrochem. Soc.* **1995**, *142*, 1431-1435.

[56] B. B. Berkes, A. Jozwiuk, M. Vračar, H. Sommer, T. Brezesinski, J. Janek, *Anal. Chem.* **2015**, *87*, 5878-5883.

[57] B. B. Berkes, A. Jozwiuk, H. Sommer, T. Brezesinski, J. Janek, *Electrochem. Commun.* **2015**, *60*, 64-69.